

# Defect-Mediated Bulk Dzyaloshinskii-Moriya Interaction in Ferromagnetic Multilayer Thin Films

Ayaka P. Ohki<sup>1,\*</sup>, Tatsuro Karino<sup>1,\*</sup>, Daigo Shimizu<sup>1</sup>, Nobuyuki Ikarashi<sup>1,2</sup>, Takeshi Kato<sup>1,2</sup>, Daiki Oshima<sup>1,†</sup>, and Masahiro Nagao<sup>1,2,‡</sup>

<sup>1</sup>Department of Electronics, Nagoya University, Nagoya 464-8603, Japan

<sup>2</sup>Institute of Materials and Systems for Sustainability, Nagoya University, Nagoya 464-8601, Japan

\*These authors contributed equally to this work.

†To whom correspondence should be addressed. [oshima.daiki.n6@f.mail.nagoya-u.ac.jp](mailto:oshima.daiki.n6@f.mail.nagoya-u.ac.jp)

‡To whom correspondence should be addressed. [nagao.masahiro@imass.nagoya-u.ac.jp](mailto:nagao.masahiro@imass.nagoya-u.ac.jp)

## Abstract

The Dzyaloshinskii-Moriya interaction (DMI) in asymmetric multilayers is crucial for spintronics. However, it is also significant even in symmetric ones, and unveiling its atomic-level origin remains an issue. We use electron microscopy to propose defect-mediated bulk DMI in Pt/Co/Pt. We find an enhancement of the net DMI by increasing sputter gas pressure. The samples have a compositional gradient, but their compositional asymmetry is weak. Our analysis suggests that the asymmetric distribution of dislocations in the compositional gradient regions generates bulk DMI. Our results indicate the importance of bulk DMI in multilayers and could facilitate the development of spintronic devices.

## Main text

In multilayer thin films, the Dzyaloshinskii-Moriya interaction (DMI) plays crucial roles in various physical phenomena, such as the stabilization of chiral domain walls (DWs) [1,2] and skyrmions [3-6], spin-orbit-torque-induced their motions [1-3,4,7-9], magnetization reversal [10,11], and nonreciprocal spin wave [12] and magnetoacoustic surface wave [13]. The inversion symmetry breaking at the interfaces between the ferromagnetic layer and the heavy metal layer with spin-orbit coupling (SOC) is essential for the emergence of the DMI.

Extensive research efforts have led to a considerable understanding of the interfacial DMI [6,14-21]. However, the microscopic mechanisms remain a central issue. It is interesting to note that the DMI is non-zero even in sputtered symmetric multilayers such as Pt/Co/Pt [22,23] and Pd/Co/Pd [24-26]. Several studies have successfully controlled the net DMI in Pt/Co/Pt by adjusting sputtering conditions during growth, such as Ar gas pressure [27], substrate temperature and chamber base pressure [28], and by irradiating Ar<sup>+</sup> ions [29]. These results imply that intermixing leads to the loss of interfaces and is detrimental to the DMI. However, recent calculations have predicted a robustness of the DMI against intermixing [30] and even an enhancement of the DMI due to intermixing [31]. Another interesting observation is a bulk DMI in films, where the compositional gradient breaks inversion symmetry [32-35]. Still, there is limited research on whether the bulk DMI can be applied to multilayer thin films [36]. In addition, recent studies have demonstrated that defects break the inversion symmetry in centrosymmetric materials, generating the DMI [37-40], but the relationship between defects and the DMI in sputtered multilayer thin films has yet to be addressed.

Elucidating the microscopic origin of significant DMI in symmetric multilayers could provide detailed insight into the nature of the DMI. However, the lack of detailed atomic-scale analysis data poses a challenge due to the polycrystalline and ultrathin nature of sputtered multilayers. We use Lorentz transmission electron microscopy (LTEM) and high-angle annular dark-field scanning transmission electron microscopy (HAADF-STEM) to investigate the origin of significant DMI in Pt/Co/Pt. Our study stresses the importance of taking defects in the compositional gradient regions into account.

We observe an enhancement of the net DMI in Pt/Co/Pt by only increasing sputter Ar gas pressure  $P$ , and the absence of interfaces, suggesting the presence of bulk DMI. However, the compositional asymmetries are weak. Our analysis unveils an asymmetric dislocation distribution. Overall, these results indicate the significant role of atomic displacements induced by defects in the compositional gradient regions for the DMI in multilayer thin films.

Multilayers of substrates/Ta(5 nm)/[Pt(1 nm)/Co(1 nm)/Pt(1 nm)]<sub>15</sub>/Pt(3 nm) were grown using magnetron sputter deposition at room temperature with  $P = 0.4, 1.0, 1.5$ , and  $2.0$  Pa. Hereafter, we describe these samples as the 0.4-, 1.0-, 1.5-, and 2.0-samples. We deposited the thin films on 10-nm and 15-nm-thick Si<sub>3</sub>N<sub>4</sub> membrane substrates used for LTEM imaging, and on thermally oxidized Si wafer substrates used for HAADF-STEM imaging and vibrating sample magnetometry measurements. These thin films on two different substrates were grown simultaneously.

We investigate the impact of increasing  $P$  on magnetic structures in perpendicularly magnetized Pt/Co/Pt. The LTEM images in Fig. 1 display the DW structures in the 0.4-, 1.0-, 1.5-, and 2.0-samples. The top and bottom images were captured at sample tilt angles of  $\alpha = 0^\circ$  and  $30^\circ$ , respectively. The bright and dark line contrasts correspond to DWs. For the 0.4-sample, pronounced DW contrasts are evident at  $\alpha = 0^\circ$  [Fig. 1(a), top], signifying the dominance of the Bloch-type DW component. In contrast, for the  $P \geq 1.0$  Pa samples, no DW contrast is observed at  $\alpha = 0^\circ$  [Figs. 1(b)–1(d), top], while the DW contrasts appear only at  $\alpha > 0^\circ$  [Figs. 1(b)–1(d), bottom], signifying the presence of the Néel-type DWs [24]. These observations indicate that the symmetric  $P \geq 1.0$  Pa samples have the substantial DMI energy values. It is important to note that our samples were deposited at a constant pressure during growth, unlike the previous study where varying pressure during growth was used to induce asymmetry and substantial DMI [27]. We estimate the critical values of the DMI energy  $|D_c|$ , which is required to stabilize chiral Néel DWs [4,41,42]

$$|D_c| = \frac{4}{\pi} \sqrt{\frac{A}{K_{\text{eff}}}} K_d, \quad (1)$$

where  $A$  is the exchange stiffness,  $K_{\text{eff}}$  is effective perpendicular magnetic anisotropy constant,  $K_d = \mu_0 M_s^2 / 2$  is the magnetostatic energy constant, and  $M_s$  is saturation magnetization. We can extract  $K_d$  and  $K_{\text{eff}}$  values from the magnetization curves. For the 1.0-, 1.5-, and 2.0-samples, the  $K_d$  values are 1.45, 1.38, and 1.28 MJ/m<sup>3</sup>, respectively, while the  $K_{\text{eff}}$  values are 0.668, 0.814, and 1.223 MJ/m<sup>3</sup>. Using  $A = 1.0$  pJ/m, we estimated  $|D_c|$  to be 2.26, 1.94, and 1.48 mJ/m<sup>2</sup> for the 1.0-, 1.5-, and 2.0-samples, respectively. Despite employing a sufficiently small  $A$  value due to a reduction of crystal quality with high  $P$  [27,43], compared to  $A = 10.0$  pJ/m for typical Co-based multilayers, the resulting  $|D_c|$  are notably large. Our estimates may be an overestimate. Nonetheless, there is no doubt that the  $P \geq 1.0$  Pa samples have the substantial  $|D_c|$ . In addition, our recent study identified an enhancement of the DMI in Pt/Co/Ta deposited at  $P = 2.0$  Pa, as evidenced by the formation of field-free skyrmions [44]. Our present and recent findings demonstrate that sputter deposition with high  $P$  enhances asymmetry and/or structural imperfections.

We use HAADF-STEM to investigate the layer and interface structures of the 0.4- and 1.0-samples at the atomic scale. The previous study on Pt/Co/Pt reported that as  $P$  increases, there is a transition at  $P = 0.8$  Pa from intermixing to well-defined interfaces [27]. However, there has been no direct observation of these structures. Aberration-corrected HAADF-STEM, which provides image contrast scaling with approximately the square of the atomic number, allows for the direct observation of the atomic-scale intermixing of Pt and Co. The low-magnification cross-sectional HAADF-STEM images in Figs. 2(a),(d) show the layer structures in the 0.4- and 1.0-samples, respectively. The 0.4-sample displays relatively flat layers and grains with a lateral size of  $L \approx 20$  nm, while the 1.0-sample exhibits the composition bending (the lattice planes

are relatively flat) and grains with  $L \approx 5\text{-}10$  nm. Additionally, both samples display random-distributed mosaic crystal states within the grains. Importantly, the 0.4- and 1.0-samples lack well-defined interfaces. Instead, we observe the compositional gradients, as depicted in Figs. 2(c),(f) through the integrated intensity profiles obtained from the rectangular regions in Figs. 2(b),(e). These profiles display sinusoidal-like modulations, contrasting with the square waves that would appear if the samples had interfaces [45]. The sharp peaks correspond to atomic columns and lattice fringes. The absence of interfaces in the 1.0-sample may be due to the composition bending [Fig. 2(d)]. Both samples show a tendency for greater intermixing around the composition bending regions such as near the grain boundaries, with a decreasing extent of intermixing away from the regions [46]. This tendency implies that intermixing extends throughout the grains in the 1.0-sample due to small grains.

Our observations demonstrate that the DMI originates from the bulk state. The enhancement of the net DMI is supposed to be induced by the combined or single factors within the framework of the three-site Fert-Levy model [47], including increased asymmetries, enhanced effective SOC, and atomic displacements. In the following, we examine these factors.

We analyze the extent of the compositional gradients in the 0.4- and 1.0-samples. We obtained intensity profiles with a width of  $w = 1.88$  nm in 114 and 122 regions for the 0.4- and 1.0-samples, respectively. We measured the compositional gradient distances  $d_u$  and  $d_l$  from the layers with the highest Pt concentration (highest Pt layers) at the top and bottom to the layers with the highest Co concentration (highest Co layers) at the middle, respectively [the insets of Figs. 3(a),(b)]. (Numerical data are listed in [46].) In the 1.0-sample, we encountered difficulties in obtaining the atomically-resolved images with statistical significance due to small polycrystalline grains, hence we used lattice images for analysis. We frequently observe two adjacent highest Co layers and highest Pt layers in the 1.0-sample, implying a shorter interdiffusion distance compared to the 0.4-sample. In that case, we adopted the closest distance between the highest Pt layer and the highest Co layer. Our analysis excluded the regions with considerable Pt diffusion. In Figs. 3(a),(b), we illustrate  $d_u$  and  $d_l$  for the individual regions in the 0.4- and 1.0-samples, showing a relatively large dispersion. The average  $d_u$  and  $d_l$  values and averaged distance differences are  $d_{u(\text{ave})} = 1.688$  nm,  $d_{l(\text{ave})} = 1.569$  nm, and  $d_{l-u(\text{ave})} = -0.119$  nm for the 0.4-sample, and  $d_{u(\text{ave})} = 1.427$  nm,  $d_{l(\text{ave})} = 1.388$  nm, and  $d_{l-u(\text{ave})} = -0.039$  nm for the 1.0-sample. The results suggest that the macroscopic compositional asymmetries are weak. In addition, the degree of the compositional asymmetry in the 1.0-sample is not much different from that in the 0.4-sample. We determine the net bulk DMI energy  $D_{\text{net}}$  based on a previous study [35], which demonstrate that the magnitude of the bulk DMI in  $\text{Co}_x\text{Pt}_{1-x}$  films is inversely proportional to the gradient distance when  $\Delta x = x_s - x_e$  is constant ( $x_s$  and  $x_e$  are the starting and ending compositions, respectively). Figures 3(c),(f) present the  $D_{\text{net}}$  dispersions, derived from the results of Figs. 3(a),(b), assuming the maximum compositional gradients ( $\Delta x = -1$  and 1). The  $D_{\text{net}}$  dispersions are large, up to  $|D_{\text{net}}| \approx 0.6$  mJ/m<sup>2</sup>, corresponding to the large dispersion of  $d_u$  and  $d_l$ . The 0.4- and 1.0-samples have the average  $D_{\text{net}}$  values of  $|D_{\text{net}(\text{ave})}| \approx 0.05$  and  $\approx 0.03$  mJ/m<sup>2</sup>, respectively. Notably, the  $D_{\text{net}(\text{ave})}$  value for the 1.0-sample is too small to explain the LTEM observations, and it is not much different from that for the 0.4-sample. Additionally, the  $D_{\text{net}(\text{ave})}$  value for the 0.4-sample is an order of magnitude smaller than the value reported in previous study [48]. In light of our results, it is clear that the compositional asymmetry is not directly responsible for the observed substantial DMI and the significant DMI reported so far.

We also examined SOC. Recent X-ray Absorption Spectroscopy (XAS) studies on Co-based and Fe-based multilayers have demonstrated an enhanced SOC in the local electronic structures of Co and Fe by measuring the branching ratio  $B = I(L_3)/[I(L_3) + I(L_2)]$  [49-52] where  $I(L_{2,3})$  is the XAS intensity at the  $L_{2,3}$  edges. The core-loss spectra in electron energy loss spectroscopy (EELS) can provide the same information as the XAS spectra. However, the  $B$  values estimated from

our EELS measurements does not show a significant enhancement of SOC in the 0.4- and 1.0-samples [46]. The remaining factor is atomic displacements induced by defects. Defects increase with increasing  $P$  [27,43], suggesting a close association between DMI and defects. We further conduct HAADF-STEM observations and analyze the positions of defects. The highly disordered grain boundaries make it challenging to identify asymmetry, and their vicinity with considerable Pt diffusion generates almost vanishing magnetization. Therefore, we focus on dislocations within the grains. Due to the aforementioned reasons, we select to focus on the 0.4-sample. Given the well-established evidence of significant DMI in sputter-deposited Pt/Co/Pt [22,23,27,28,48], we expect our 0.4-sample to exhibit significant DMI. Our HAADF-STEM observations unveil that dislocations are present in considerable quantity. Figure 4(a) shows a representative Fourier-filtered HAADF-STEM image, displaying streak-like blurred contrasts between two atomic column contrasts, as indicated by the yellow-green arrows. The streak-like contrasts are observed mainly parallel to the layers. Figure 4(b) shows the intensity profiles along the 1-1' to 4-4' lines in Fig. 4(a), proving the presence of these streak-like blurred contrasts. The intensity profile along 5-5' line is an example of streak-contrast-free profiles. These streak-like contrasts can be identified as resulting from screw [Fig. 4(c)], edge [Fig. 4(d)], and mixed dislocations. We analyze the positional distribution of 241 dislocations relative to the highest Co layers. As exemplified in the right panel in Fig. 4(a), the intensity profiles combined with HAADF-STEM images can simultaneously identify the position of the layers with dislocations ( $N_d$ ) and the highest-Co layers ( $N_{Co}$ ). We counted the number of layers starting from the bottom highest Pt layers, and excluded the layers with dislocations within three layers counting from the top and bottom highest Pt layers, presuming them to be almost non-magnetic regions [35]. The analysis of the layer differences  $N_{d-Co}$  ( $= N_d - N_{Co}$ ) is shown in Fig. 4(e), where the ratios of positive, negative, and zero values are 51.8%, 26.6%, and 21.6%, respectively. (Numerical data are listed in [46].) The number of layers with dislocations above the highest Co layer is more than those below, indicating that the dislocation distribution is biased. Our result suggests that the asymmetric dislocation distribution in the compositional gradient regions gets involved in the net bulk DMI.

For magnetic metallic systems, the three-site Fert-Levy model effectively captures the microscopic nature of the DMI vector between neighboring magnetic atoms, mediated by the surrounding heavy atoms. As illustrated in Fig. 4(f), this model is represented by three vectors on the side of the triangle and an angle of the heavy metal atom side. Thus, atomic displacements modify the DMI vector. Recent experimental observations have demonstrated that displacements of Co and Pt atoms induced by uniaxial strain can change the net DMI vector in Pt/Co/Pt almost twofold [48]. Dislocations similarly produce displacements of Co and Pt atoms around the dislocation lines [the light-blue shade regions in Figs. 4(c),(d)], leading to a change in the DMI vector. In the samples deposited with higher  $P$ , the difference in Pt concentration between the upper and lower layers for dislocations widens, which may result in a more pronounced net DMI. In addition, the atomic displacements around the dislocation lines can also impact the degree of 3d-5d orbital hybridization near the Fermi energy, which correlates with the DMI [16]. However, a detailed theoretical study of the impact of dislocations in the compositional gradient regions on the DMI is required to fully understand the origin of the DMI in sputtered multilayers. Although we could not determine dislocation-type-dependent distributions with sufficient statistical significance, the impact on the DMI likely vary depending on the dislocation types. Additionally, the asymmetrical strain field distributions observed may have associations with other physical phenomena. Recent findings indicate that symmetrical bulk FeNi alloys manifest substantial bulk spin-orbit torque induced by asymmetric strain field distributions [53]. Thus, our results could yield novel insights into spin-orbit physics in sputtered multilayer thin films.

In conclusion, our study shed light on defects as the origin of the DMI in sputtered multilayer thin films for the first time.

We observe substantial net DMI in Pt/Co/Pt simply by increasing the sputter-deposition Ar gas pressure and demonstrate the presence of bulk DMI. While the compositional asymmetries are weak and not directly responsible for the net DMI, our HAADF-STEM observations unveil a biased dislocation distribution, strongly suggesting the presence of bulk DMI mediated by defects in the composition gradient regions. Our results indicate the potential for designing the DMI through internal strains and offer new insights into spin-orbit physics in sputter-deposition multilayer thin films.

## References

- [1] S. Emori, U. Bauer, S. M. Ahn, E. Martinez, and G. S. Beach, Current-driven dynamics of chiral ferromagnetic domain walls, *Nat. Mater.* **12**, 611 (2013).
- [2] K. S. Ryu, L. Thomas, S. H. Yang, and S. Parkin, Chiral spin torque at magnetic domain walls, *Nat. Nanotechnol.* **8**, 527 (2013).
- [3] W. Jiang, P. Upadhyaya, W. Zhang, G. Yu, M. B. Jungfleisch, F. Y. Fradin, J. E. Pearson, Y. Tserkovnyak, K. L. Wang, O. Heinonen, S. G. E. te Velthuis, and A. Hoffmann, Blowing magnetic skyrmion bubbles, *Science* **349**, 283 (2015).
- [4] S. Woo, K. Litzius, B. Krüger, M. Im, L. Caretta, K. Richter, M. Mann, A. Krone, R. Reeve, M. Weigand, P. Agrawal, I. Lemesh, M. Mawass, Peter. Fischer, M. Kläui, and G. S. D. Beach, Observation of room-temperature magnetic skyrmions and their current-driven dynamics in ultrathin metallic ferromagnets, *Nat. Mater.* **15**, 501 (2016).
- [5] C. Moreau-Luchaire, C. Moutafis, N. Reyren, J. Sampaio, C. A. F. Vaz, N. Van Horne, K. Bouzehouane, K. Garcia, C. Deranlot, P. Warnicke, P. Wohlhüter, J.-M. George, M. Weigand, J. Raabe, V. Cros, and A. Fert, Additive interfacial chiral interaction in multilayers for stabilization of small individual skyrmions at room temperature, *Nat. Nanotechnol.* **11**, 444 (2013).
- [6] O. Boulle, J. Vogel, H. Yang, S. Pizzini, D. de Souza Chaves, A. Locatelli, T. O. Menteş, A. Sala, L. D. Buda-Prejbeanu, O. Klein, M. Belmeguenai, Y. Roussigné, A. Stashkevich, S. M. Chérif, L. Aballe, M. Foerster, M. Chshiev, S. Auffret, I. M. Miron, and G. Gaudin, Room-temperature chiral magnetic skyrmions in ultrathin magnetic nanostructures, *Nat. Nanotechnol.* **11**, 449 (2016).
- [7] G. Chen, T. Ma, A. T. N'Diaye, H. Kwon, C. Won, Y. Wu, and A. K. Schmid, Tailoring the chirality of magnetic domain walls by interface engineering, *Nat. Commun.* **4**, 1 (2013).
- [8] O. Boulle, S. Rohart, L.D. Buda-Prejbeanu, E. Jue, I. M. Miron, S. Pizzini, J. Vogel, G. Gaudin, and A. Thiaville, Domain Wall Tilting in the Presence of the Dzyaloshinskii-Moriya Interaction in Out-of-Plane Magnetized Magnetic Nanotrails, *Phys. Rev. Lett.* **111**, 217203 (2013).
- [9] G. Yu, P. Upadhyaya, X. Li, W. Li, S. K. Kim, Y. Fan, K. L. Wong, Y. Tserkovnyak, P. K. Amiri, and K. L. Wang, Room-Temperature Creation and Spin–Orbit Torque Manipulation of Skyrmions in Thin Films with Engineered Asymmetry, *Nano Lett.* **16**, 1981 (2016).
- [10] H. Imamura, T. Nozaki, S. Yuasa, and Y. Suzuki, Deterministic Magnetization Switching by Voltage Control of Magnetic Anisotropy and Dzyaloshinskii-Moriya Interaction under an In-Plane Magnetic Field, *Phys. Rev. Appl.* **10**, 054039 (2018).
- [11] H. Wu, J. Nance, S. A. Razavi, D. Lujan, B. Dai, Y. Liu, H. He, B. Cui, D. Wu, K. Wong, K. Sobotkiewich, X. Li, G. P. Carman, and K. L. Wang, Chiral symmetry breaking for deterministic switching of perpendicular magnetization by spin-orbit torque, *Nano Lett.* **21**, 515 (2021).
- [12] H. Wang, J. Chen, T. Liu, J. Zhang, K. Baumgaertl, C. Guo, Y. Li, C. Liu, P. Che, S. Tu, S. Liu, P. Gao, X. Han, D.

- Yu, M. Wu, D. Grundler, and H. Yu, Chiral Spin-Wave Velocities Induced by All-Garnet Interfacial Dzyaloshinskii-Moriya Interaction in Ultrathin Yttrium Iron Garnet Films, *Phys. Rev. Lett.* **124**, 027203 (2020).
- [13] M. Küß, M. Heigl, L. Flacke, A. Hörner, M. Weiler, M. Albrecht, and A. Wixforth, Nonreciprocal Dzyaloshinskii-Moriya Magnetoacoustic Waves, *Phys. Rev. Lett.* **125**, 217203 (2020).
- [14] K.-W. Kim, H.-W. Lee, K.-J. Lee, and M. D. Stiles, Chirality from Interfacial Spin-Orbit Coupling Effects in Magnetic Bilayers, *Phys. Rev. Lett.* **111**, 216601 (2013)
- [15] H. X. Yang, A. Thiaville, S. Rohart, A. Fert, and M. Chshiev, Anatomy of Dzyaloshinskii-Moriya Interaction at Co/Pt Interfaces, *Phys. Rev. Lett.* **115**, 267210 (2015).
- [16] A. Belabbes, G. Bihlmayer, F. Bechstedt, S. Blügel, and A. Manchon, Hund's Rule-Driven Dzyaloshinskii-Moriya Interaction at 3d–5d Interfaces, *Phys. Rev. Lett.* **117**, 247202 (2016).
- [17] M. Hoffmann, B. Zimmermann, G. P. Müller, D. Schürhoff, N. S. Kiselev, C. Melcher, and S. Blügel, Antiskyrmions stabilized at interfaces by anisotropic Dzyaloshinskii-Moriya interactions, *Nat. Commun.* **8**, 308 (2017).
- [18] H. Yang, G. Chen, A. A. C. Cotta, A. T. N'Diaye, S. A. Nikolaev, E. A. Soares, W. A. A. Macedo, K. Liu, A. K. Schmid, A. Fert, and M. Chshiev, Significant Dzyaloshinskii-Moriya interaction at graphene-ferromagnet interfaces due to the Rashba effect, *Nat. Mater.* **17**, 605 (2018).
- [19] B. Yang, Q. Cui, J. Liang, M. Chshiev, and H. Yang, Reversible control of Dzyaloshinskii-Moriya interaction at the graphene/Co interface via hydrogen absorption, *Phys. Rev. B* **101**, 014406 (2020).
- [20] C. Deger, Strain-enhanced Dzyaloshinskii–Moriya interaction at Co/Pt interfaces, *Sci. Rep.* **10**, 12314 (2020).
- [21] H. Yang, J. Liang, and Q. Cui, First-principles calculations for Dzyaloshinskii–Moriya interaction, *Nat. Rev. Phys.* **5**, 43 (2023).
- [22] A. Hrabec, N. A. Porter, A. Wells, M. J. Benitez, G. Burnell, S. McVitie, D. McGrouther, T. A. Moore, and C. H. Marrows, Measuring and tailoring the Dzyaloshinskii-Moriya interaction in perpendicularly magnetized thin films, *Phys. Rev. B* **90**, 020402(R) (2014).
- [23] S.-G. Je, D.-H. Kim, S.-C. Yoo, B.-C. Min, K.-J. Lee, and S.-B. Choe, Asymmetric magnetic domain-wall motion by the Dzyaloshinskii-Moriya interaction, *Phys. Rev. B* **88**, 214401 (2013).
- [24] S. D. Pollard, J. A. Garlow, J. Yu, Z. Wang, Y. Zhu, and H. Yang, Observation of stable Néel skyrmions in cobalt/palladium multilayers with Lorentz transmission electron microscopy, *Nat. Commun.* **8**, 14761 (2017).
- [25] J. Brandão, D. A. Dugato, R. L. Seeger, J. C. Denardin, T. J. A. Mori, and J. C. Cezar, Observation of magnetic skyrmions in unpatterned symmetric multilayers at room temperature and zero magnetic field, *Sci. Rep.* **9**, 4144 (2019).
- [26] Y. Wei, C. Liu, Z. Zeng, X. Wang, J. Wang, and Q. Liu, Room-temperature zero field and high-density skyrmions in Pd/Co/Pd multilayer films, *J. Magn. Magn. Mater.* **521**, 167507 (2021).
- [27] R. Lavrijsen, D. M. F. Hartmann, A. van den Brink, Y. Yin, B. Barcones, R. A. Duine, M. A. Verheijen, H. J. M. Swagten, and B. Koopmans, Asymmetric magnetic bubble expansion under in-plane field in Pt/Co/Pt: Effect of interface engineering, *Phys. Rev. B* **91**, 104414 (2015).
- [28] A. W. J. Wells, P. M. Shepley, C. H. Marrows, and T. A. Moore, Effect of interfacial intermixing on the Dzyaloshinskii-Moriya interaction in Pt/Co/Pt, *Phys. Rev. B* **95**, 054428 (2017).
- [29] A. L. Balk, K.-W. Kim, D. T. Pierce, M. D. Stiles, J. Unguris, and S. M. Stavis, Simultaneous control of the Dzyaloshinskii-Moriya interaction and magnetic anisotropy in nanomagnetic trilayers, *Phys. Rev. Lett.* **119**, 077205

(2017).

- [30] B. Zimmermann, W. Legrand, D. Maccariello, N. Reyren, V. Cros, S. Blügel, and A. Fert, Dzyaloshinskii-Moriya interaction at disordered interfaces from ab initio theory: Robustness against intermixing and tunability through dusting, *Appl. Phys. Lett.* **113**, 232403 (2018).
- [31] P. C. Carvalho, I. P. Miranda, J. Brandão, A. Bergman, J. C. Cezar, A. B. Klautau, and H. M. Petrilli, Correlation of Interface Interdiffusion and Skyrmionic Phases, *Nano Lett.* **23**, 4854 (2023).
- [32] D-H. Kim, M. Haruta, H-W. Ko, G. Go, H-J. Park, T. Nishimura, D-Y. Kim, T. Okuno, Y. Hirata, Y. Futakawa, H. Yoshikawa, W. Ham, S. Kim, H. Kurata, A. Tsukamoto, Y. Shiota, T. Moriyama, S-B. Choe, K-J. Lee, and T. Ono, Bulk Dzyaloshinskii–Moriya interaction in amorphous ferrimagnetic alloys, *Nat. Mater.* **18**, 685 (2019).
- [33] S. Krishnia, E. Haltz, L. Berges, L. Aballe, M. Foerster, L. Bocher, R. Weil, A. Thiaville, J. Sampaio, and A. Mougin, Spin-Orbit Coupling in Single-Layer Ferrimagnets: Direct Observation of Spin-Orbit Torques and Chiral Spin Textures, *Phys. Rev. Applied* **16**, 024040 (2021).
- [34] J. Liang, M. Chshiev, A. Fert, and H. Yang, Gradient-Induced Dzyaloshinskii–Moriya Interaction, *Nano Lett.* **22**, 10128 (2022).
- [35] Q. Zhang, J. Liang, K. Bi, L. Zhao, H. Bai, Q. Cui, H. A. Zhou, H. Bai, H. Feng, W. Song, G. Chai, O. Gladilin, H. Schultheiss, T. Zhu, J. Zhang, Y. Peng, H. Yang, and W. Jiang, Quantifying the Dzyaloshinskii–Moriya interaction induced by the bulk magnetic asymmetry, *Phys. Rev. Lett.* **128**, 167202 (2022).
- [36] J. Park, T. Kim, G. W. Kim, V. Bessonov, A. Telegin, I. G. Iliushin, A. A. Pervishko, D. Yudin, A. Y. Samardak, A. V. Ognev, A. S. Samardak, J. Cho, and Y. K. Kim, Compositional gradient induced enhancement of Dzyaloshinskii–Moriya interaction in Pt/Co/Ta heterostructures modulated by Pt–Co alloy intralayers, *Acta Mater.* **241**, 118383 (2022).
- [37] A. Michels, D. Mettus, I. Titov, A. Malyeyev, M. Bersweiler, P. Bender, I. Peral, R. Birringer, Y. Quan, P. Hautle, and J. Kohlbrecher, Microstructural-defect-induced Dzyaloshinskii–Moriya interaction, *Phys. Rev. B* **99**, 014416 (2019).
- [38] A. Chakraborty, A. K. Srivastava, A. K. Sharma, A. K. Gopi, K. Mohseni, A. Ernst, H. Deniz, B. K. Hazra, S. Das, P. Sessi, and I. Kostanovskiy, Magnetic skyrmions in a thickness tunable 2D ferromagnet from a defect driven Dzyaloshinskii–Moriya interaction, *Adv. Mater.* **34**, 2108637 (2022).
- [39] Z. Li, H. Zhang, G. Li, J. Guo, Q. Wang, Y. Deng, Y. Hu, X. Hu, C. Liu, M. Qin, X. Shen, R. Yu, X. Gao, Z. Liao, J. Liu, Z. Hou, Y. Zhu, and X. Fu, Room-temperature sub-100 nm Néel-type skyrmions in non-stoichiometric van der Waals ferromagnet  $\text{Fe}_{3-x}\text{GaTe}_2$  with ultrafast laser writability, *Nat. Commun.* **15**, 1017 (2024).
- [40] C. Zhang, Z. Jiang, J. Jiang, W. He, J. Zhang, F. Hu, S. Zhao, D. Yang, Y. Liu, Y. Peng, H. Yang, and H. Yang, Above-room-temperature chiral skyrmion lattice and Dzyaloshinskii–Moriya interaction in a van der Waals ferromagnet  $\text{Fe}_{3-x}\text{GaTe}_2$ , *Nat. Commun.* **15**, 4472 (2024).
- [41] A. Thiaville, S. Rohart, É. Jué, V. Cros, and A. Fert, Dynamics of Dzyaloshinskii domain walls in ultrathin magnetic films, *EPL* **100**, 57002 (2012).
- [42] Y. Wu, S. Zhang, J. Zhang, W. Wang, Y. L. Zhu, J. Hu, G. Yin, K. Wong, C. Fang, C. Wan, X. Han, Q. Shao, T. Taniguchi, K. Watanabe, J. Zang, Z. Mao, X. Zhang, and K. L. Wang, Néel-type skyrmion in  $\text{WTe}_2/\text{Fe}_3\text{GeTe}_2$  van der Waals heterostructure, *Nat. Commun.* **11**, 3860 (2020).
- [43] R. Messier, A. P. Giri, and R. A. Roy, Revised structure zone model for thin film physical structure, *J. Vac. Sci. Technol. A* **2**, 500 (1984)
- [44] T. Karino, D. Shimizu, A. P. Ohki, N. Ikarashi, T. Kato, D. Oshima, and M. Nagao, Domain-stored skyrmion structures

for a reading error-detectable racetrack memory, arXiv

- [45] I.-H. Kao, R. Muzzio, H. Zhang, M. Zhu, J. Gobbo, S. Yuan, D. Weber, R. Rao, J. Li, J. H. Edgar, J. E. Goldberger, J. Yan, D. G. Mandrus, J. Hwang, R. Cheng, J. Katoch, and S. Singh, Deterministic switching of a perpendicularly polarized magnet using unconventional spin–orbit torques in WTe<sub>2</sub>, *Nat. Mater.* **21**, 1029 (2022).
- [46] See Supplemental Material
- [47] A. Fert and P. M. Levy, Role of Anisotropic Exchange Interactions in Determining the Properties of Spin-Glasses, *Phys. Rev. Lett.* **44**, 1538 (1980).
- [48] N. S. Gusev, A. V. Sadovnikov, S. A. Nikitov, M. V. Sapozhnikov, and O. G. Udalov, Manipulation of the Dzyaloshinskii–Moriya Interaction in Co/Pt Multilayers with Strain, *Phys. Rev. Lett.* **124**, 157202 (2020).
- [49] J. W. Lee, Y.-W. Oh, S.-Y. Park, A. I. Figueroa, G. van der Laan, G. Go, K.-J. Lee, and B.-G. Park, Enhanced spin-orbit torque by engineering Pt resistivity in Pt/Co/AlO<sub>x</sub> structures, *Phys. Rev. B* **96**, 064405 (2017).
- [50] R. Wang, Z. Xiao, H. Liu, Z. Quan, X. Zhang, M. Wang, M. Wu, and X. Xu, Enhancement of perpendicular magnetic anisotropy and spin-orbit torque in Ta/Pt/Co/Ta multi-layered heterostructures through interfacial diffusion, *Appl. Phys. Lett.* **114**, 042404 (2019).
- [51] D. K. Ojha, R. Chatterjee, Y.-L. Lin, Y.-H. Wu, P.-W. Chen, and Y.-C. Tseng, Spin-torque efficiency enhanced in sputtered topological insulator by interface engineering, *J. Magn. Magn. Mater.* **572**, 170638 (2023).
- [52] L. Chen, K. Zhang, B. Li, B. Hong, W. Huang, Y. He, X. Feng, Z. Zhang, K. Lin, W. Zhao, and Y. Zhang, Engineering Symmetry Breaking Enables Efficient Bulk Spin-Orbit Torque-Driven Perpendicular Magnetization Switching, *Adv. Funct. Mater.* **34**, 2308823 (2023).
- [53] R. E. Maizel, S. Wu, P. P. Balakrishnan, A. J. Grutter, C. J. Kinane, A. J. Caruana, P. Nakarmi, B. Nepal, D. A. Smith, Y. Lim, J. L. Jones, W. C. Thomas, J. Zhao, F. M. Michel, T. Mewes, and S. Emori, Vertically Graded FeNi Alloys with Low Damping and a Sizeable Spin-Orbit Torque, arXiv:2406.09874v1.

## Acknowledgment

We thank Y. Yamamoto, K. Higuchi, and H. Cheong for technical support of experiments. This work was financially supported by Grant-in-Aid for Scientific Research (B) (JSPS, 21H01029). This work was conducted at Microstructure Analysis Platform and Microstructure Analysis Platform in the Next-generation biomaterials Hub, Nagoya University, supported by "Advanced Research Infrastructure for Materials and Nanotechnology in Japan (ARIM)" of the Ministry of Education, Culture, Sports, Science and Technology (MEXT).

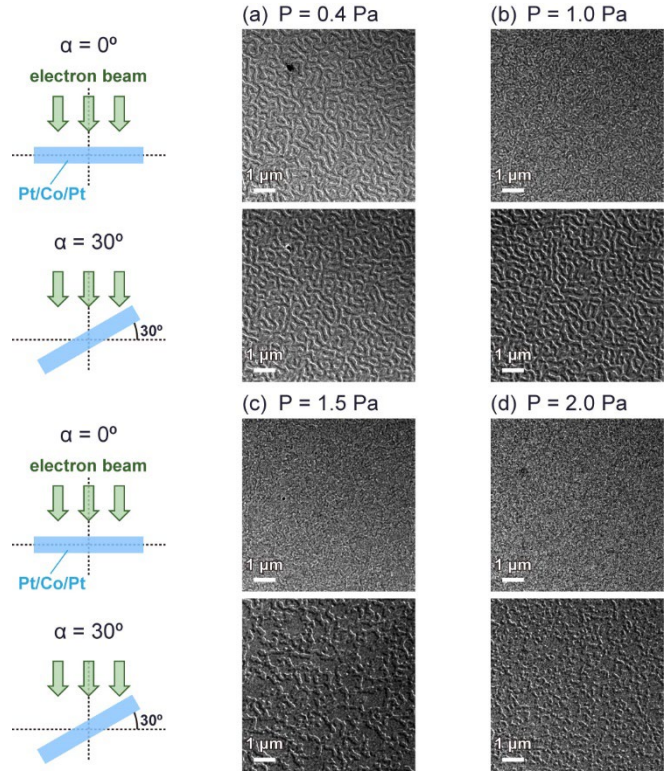


FIG. 1. LTEM images of DWs in the samples deposited with  $P = 0.4$  (a),  $1.0$  (b),  $1.5$  (c), and  $2.0$  Pa (d). The top and bottom images were captured at  $\alpha = 0^\circ$  and  $30^\circ$ , respectively.

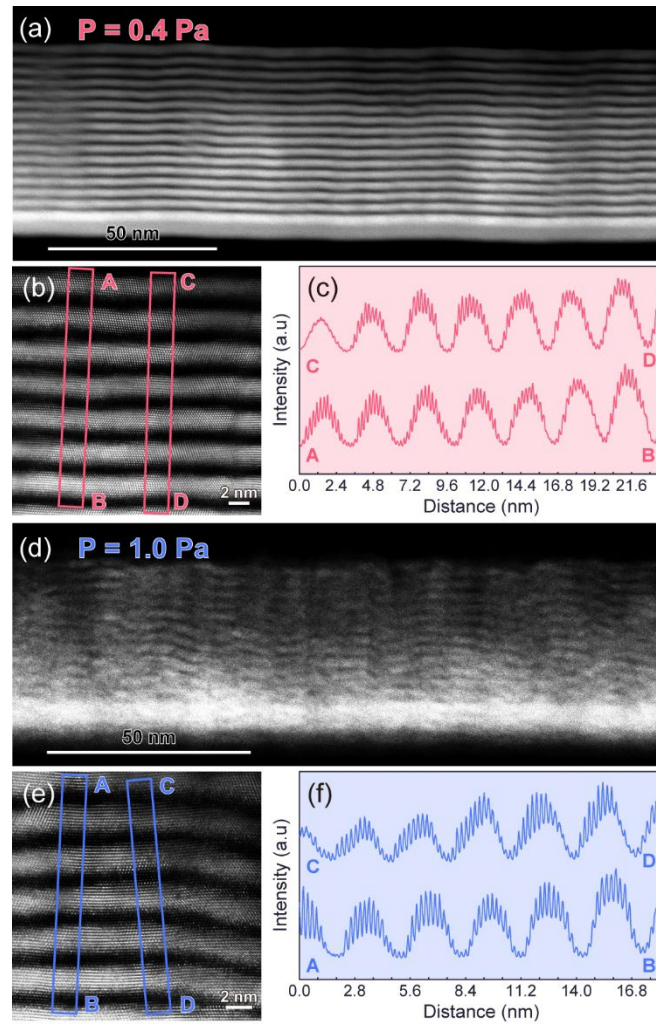


FIG. 2. Low- and high-magnification cross-sectional HAADF-STEM images in the 0.4-sample (a),(b) and the 1.0-sample (d),(e). (c),(f) Intensity profiles obtained from the rectangular regions along A-B and C-D in (b),(e).

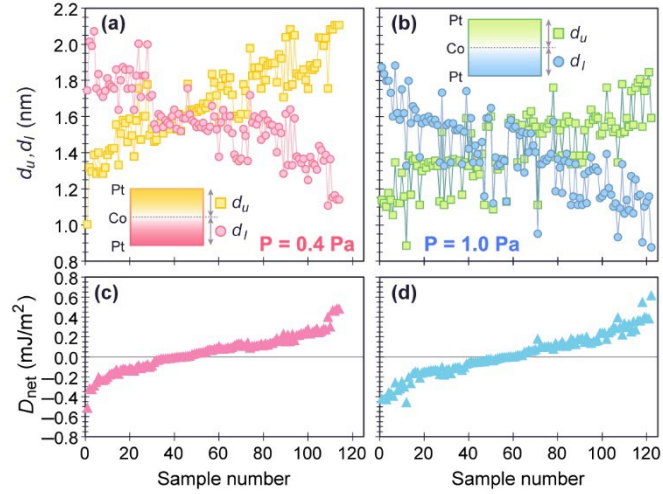


FIG. 3. Compositional gradient distances  $d_u$  (squares) and  $d_l$  (circles) for the individual regions. Intensity profiles were obtained using  $w = 1.88 \text{ nm}$  in 114 and 122 regions for the 0.4-sample (a) and 1.0-sample (b) respectively. The insets depict the definitions of  $d_u$  and  $d_l$ . (c),(d) Net bulk DMI energy  $D_{\text{net}}$  in the individual regions corresponding to (a) and (b), respectively. The calculations are based on a previous study on  $\text{Co}_x\text{Pt}_{1-x}$  films [35]. We assume the maximum compositional gradients  $\Delta x = -1$  and 1.

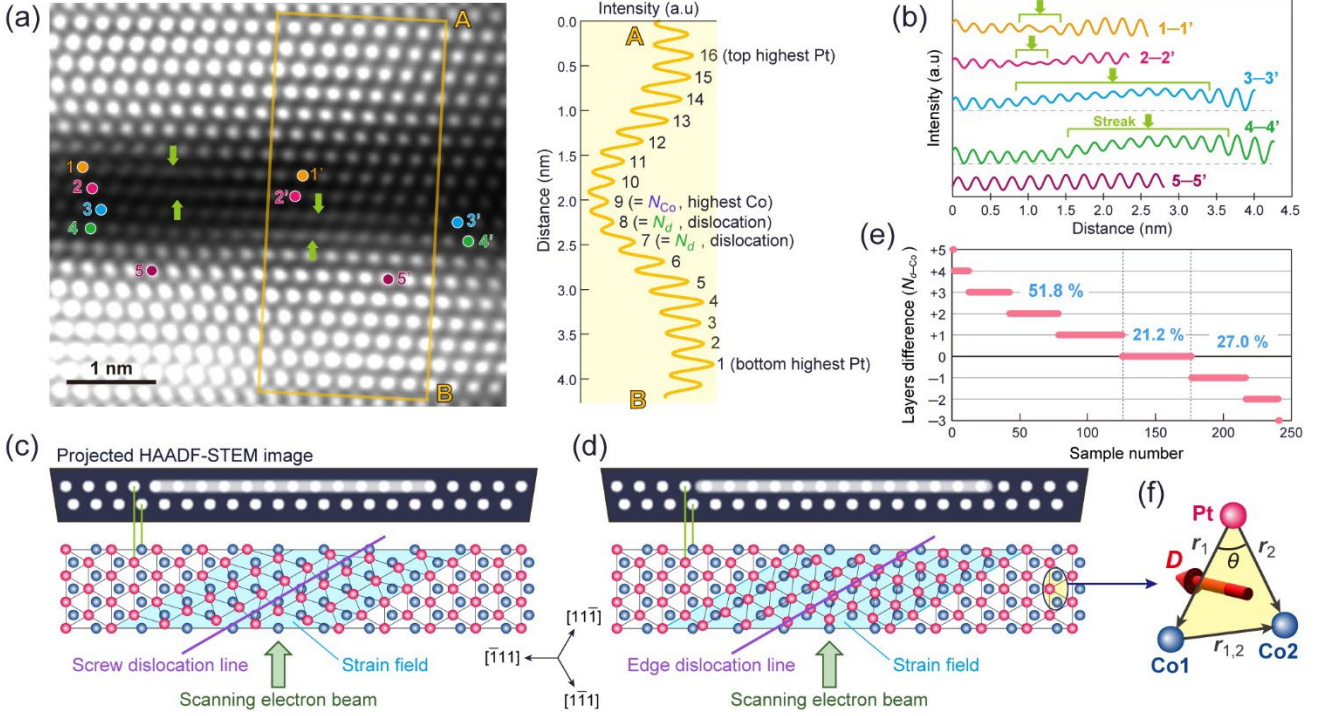


FIG. 4. Dislocation position analysis for the 0.4-sample. (a) Left: A representative Fourier-filtered HAADF-STEM image. The yellow-green arrows point to streak-like blurred contrasts. Right: Intensity profile obtained from the rectangular regions along A-B in the left image. (b) Intensity profiles along the 1-1' to 4-4' lines in (a). Intensity profile along the 5-5' line is an example of streak-contrast-free profile. (c),(d) Schematics of screw and edge dislocations, respectively. The top panels depict the schematics of the projected HAADF-STEM image. (e) Analysis of the layer differences  $N_{d-Co} = N_d - N_{Co}$ .  $N_d$  and  $N_{Co}$  represent the positions of the layer with dislocations and the highest-Co layer, respectively, counting from the bottom highest Pt layer. (f) Schematic of the three-site Fert-Levy model.  $\mathbf{D}$  is the DMI vector.

**Supplemental Material for “Defect-Mediated Bulk Dzyaloshinskii-Moriya Interaction in Ferromagnetic Multilayer Thin Films”**

Ayaka P. Ohki<sup>1</sup>, Tatsuro Karino<sup>1</sup>, Daigo Shimizu<sup>1</sup>, Nobuyuki Ikarashi<sup>1,2</sup>, Takeshi Kato<sup>1,2</sup>, Daiki Oshima<sup>1</sup>, and Masahiro Nagao<sup>1,2</sup>

<sup>1</sup> Department of Electronics, Nagoya University, Nagoya 464-8603, Japan

<sup>2</sup> Institute of Materials and Systems for Sustainability, Nagoya University, Nagoya 464-8601, Japan

## CONTENTS

- I. Considerable intermixing near the grain boundaries and the composition bending regions
- II. Numerical data of various distance measurements and number of layers for the 0.4- and 1.0-samples
- III. Separation distance between the positions of the highest Co and dislocations for the 0.4-sample
- IV. Measurements of spin-orbit coupling by electron energy loss spectroscopy for the 0.4- and 1.0-samples

### I. Considerable intermixing near the grain boundaries and the composition bending regions

We observe considerable intermixing near the grain boundaries and the composition bending region in the 0.4- and 1.0-samples. Figures S1(a)-(d) and S1(e)-(h) display HAADF-STEM images of the 0.4- and 1.0-samples, respectively. The yellow arrows indicate the location of the grain boundaries, and the blue squares enclose the regions of the compositional bending. Considerable intermixing occurs near the grain boundaries in both the 0.4- and 1.0-samples. In the 1.0-sample, the compositional bending near the grain boundary is particularly noticeable. (The lattice planes are relatively flat.) On the other hand, as depicted in Fig. S1(d), intermixing also occurs near the grain boundaries where the compositional bending is less, suggesting that intermixing near the grain boundaries is inherent regardless of the compositional bending. The extent of intermixing decreases away from the grain boundaries. The compositional bending regions are observed within the grains, leading to intermixing.

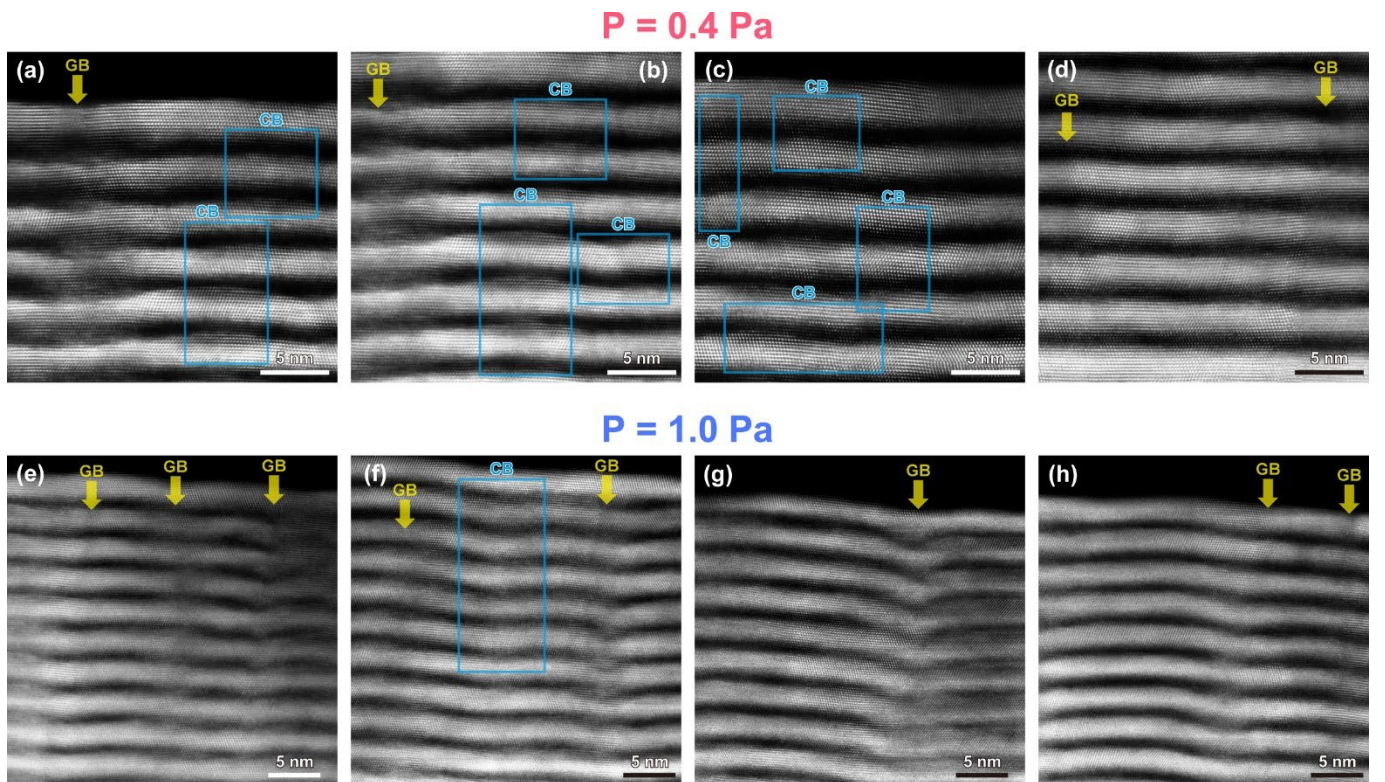


FIG. S1. HAADF-STEM images in the 0.4-sample (a)-(d) and the 1.0-sample (e)-(h). The yellow arrows indicate the location of the grain boundaries (GBs), and the blue squares enclose the regions of the compositional bending (CB).

## II. Numerical data of various distance measurements and number of layers for the 0.4- and 1.0-samples

Table S1. Numerical data of various distance measurements for the 0.4-sample. Deletion of duplicates is due to the presence of two or more dislocations in a single line profile. The sample numbers of Fig. 3(a) in the main text are rearranged in order of increasing  $d_{l-u}$  value to make the dispersion easier to recognize.

Sample number	Distance between the highest Pt at top and bottom	Remove duplicates from the left column	Distance of dislocations from the bottom highest Pt	Distance of the highest Co from the bottom highest Pt	Remove duplicates from the left column	Distance of the highest Co from the top highest Pt	Distance between $d_l$ and $d_u$	Net Bulk DMI energy [Fig. 3(c)]	Distance between dislocations and the highest Co
	$d_{\text{Pt-Pt}}$ [nm]	$d_{\text{Pt-Pt}}$ [nm]	$d_d$ [nm]	$d_{\text{Co}}$ [nm]	$d_l$ [nm]	$d_u$ [nm]	$d_{l-u}$ [nm]	$D_{\text{net}}$ [mJ/m <sup>2</sup> ]	$d_{d-\text{Co}}$ [nm]
1	2.993	2.993	2.145	1.709	1.709	1.284	0.425	-0.23	0.436
2	2.993		1.933	1.709					0.224
3	3.205	3.205	1.496	1.708	1.708	1.497	0.211	-0.10	-0.212
4	3.205		1.296	1.708					-0.412
5	3.181	3.181	2.557	1.708	1.708	1.473	0.235	-0.11	0.849
6	3.181		2.333	1.708					0.625
7	3.431	3.431	1.709	1.509	1.509	1.922	-0.413	0.17	0.2
8	3.415	3.415	2.132	1.519	1.519	1.896	-0.377	0.16	0.613
9	3.415		1.92	1.519					0.401
10	3.415		1.719	1.519					0.2
11	3.415		1.519	1.519					0
12	3.415		1.319	1.519					-0.2
13	3.227	3.227	2.12	1.472	1.472	1.755	-0.283	0.13	0.648
14	3.227		1.908	1.472					0.436
15	3.227		1.684	1.472					0.212
16	2.991	2.991	1.472	1.284	1.284	1.707	-0.423	0.23	0.188
17	2.991		1.284	1.284					0
18	2.991		1.107	1.284					-0.177
19	3.002	3.002	1.248	1.248	1.248	1.754	-0.506	0.28	0
20	3.002		1.048	1.248					-0.2
21	3.229	3.229	2.581	1.508	1.508	1.721	-0.213	0.10	1.073
22	3.229		2.357	1.508					0.849
23	3.229		1.993	1.508					0.485
24	3.229		1.508	1.508					0

25	3.229		1.308	1.508					-0.2
26	3.229		1.096	1.508					-0.412
27	3.002	3.002	2.154	1.531	1.531	1.471	0.06	-0.03	0.623
28	3.002		1.943	1.531					0.412
29	3.002		1.731	1.531					0.2
30	3.264	3.264	2.097	1.638	1.638	1.626	0.012	-0.01	0.459
31	2.965	2.965	1.141	1.365	1.365	1.6	-0.235	0.13	-0.224
32	2.965		0.918	1.365					-0.447
33	3.451	3.451	1.119	1.555	1.555	1.896	-0.341	0.14	-0.436
34	3.461	3.461	1.366	1.589	1.589	1.872	-0.283	0.11	-0.223
35	3.226	3.226	1.589	1.366	1.366	1.86	-0.494	0.23	0.223
36	3.226		1.366	1.366					0
37	3.2	3.2	1.341	1.341	1.341	1.859	-0.518	0.25	0
38	3.2		1.129	1.341					-0.212
39	3.2		0.918	1.341					-0.423
40	2.981	2.981	1.59	1.367	1.367	1.614	-0.247	0.13	0.223
41	3.494	3.494	2.318	1.659	1.659	1.835	-0.176	0.07	0.659
42	3.494		2.094	1.659					0.435
43	3.494		1.882	1.659					0.223
44	3.494		1.212	1.659					-0.447
45	3.759	3.759	2.758	2.003	2.003	1.756	0.247	-0.08	0.755
46	3.759		2.487	2.003					0.484
47	3.759		2.239	2.003					0.236
48	3.777	3.777	2	2	2	1.777	0.223	-0.08	0
49	2.748	2.748	2.475	1.745	1.745	1.003	0.742	-0.51	0.73
50	2.748		1.98	1.745					0.235
51	3.697	3.697	1.26	1.719	1.719	1.978	-0.259	0.09	-0.459
52	3.475	3.475	1.437	1.437	1.437	2.038	-0.601	0.25	0
53	3.389	3.389	1.6	1.6	1.6	1.789	-0.189	0.08	0
54	2.942	2.942	1.789	1.353	1.353	1.589	-0.236	0.13	0.436
55	2.942		1.153	1.353					-0.2
56	2.942		0.93	1.353					-0.423
57	3.204	3.204	2.25	1.567	1.567	1.637	-0.07	0.03	0.683
58	3.192	3.192	1.19	1.366	1.366	1.826	-0.46	0.22	-0.176
59	3.214	3.214	1.754	1.754	1.754	1.46	0.294	-0.14	0
60	3.194	3.194	2.145	1.521	1.521	1.673	-0.152	0.07	0.624
61	3.194		1.945	1.521					0.424
62	3.194		1.733	1.521					0.212

63	3.18	3.18	1.531	1.531	1.531	1.649	-0.118	0.06	0
64	3.18		1.319	1.531					-0.212
65	3.19	3.19	2.378	1.766	1.766	1.424	0.342	-0.16	0.612
66	3.19		2.178	1.766					0.412
67	3.19		1.966	1.766					0.2
68	3.252	3.252	2.18	1.756	1.756	1.496	0.26	-0.12	0.424
69	3.252		1.756	1.756					0
70	3.287	3.287	2.639	1.991	1.991	1.296	0.695	-0.32	0.648
71	3.287		2.427	1.991					0.436
72	3.287		1.991	1.991					0
73	3.287		1.779	1.991					-0.212
74	3.204	3.204	1.343	1.556	1.556	1.648	-0.092	0.04	-0.213
75	3.191	3.191	1.778	1.778	1.778	1.413	0.365	-0.18	0
76	3.018	3.018	1.556	1.556	1.556	1.462	0.094	-0.05	0
77	3.018		1.332	1.556					-0.224
78	3.018		1.108	1.556					-0.448
79	3.06	3.06	2.178	1.742	1.742	1.318	0.424	-0.22	0.436
80	3.06		1.954	1.742					0.212
81	3.178	3.178	1.954	1.754	1.754	1.424	0.33	-0.16	0.2
82	3.027	3.027	2.391	1.731	1.731	1.296	0.435	-0.23	0.66
83	3.049	3.049	1.966	1.542	1.542	1.507	0.035	-0.02	0.424
84	3.049		1.319	1.542					-0.223
85	3.061	3.061	2.19	1.531	1.531	1.53	0.001	0.00	0.659
86	3.061		1.978	1.531					0.447
87	3.061		1.766	1.531					0.235
88	3.487	3.487	1.543	1.543	1.543	1.944	-0.401	0.16	0
89	3.487		1.319	1.543					-0.224
90	3.04	3.04	1.98	1.756	1.756	1.284	0.472	-0.25	0.224
91	3.04		1.756	1.756					0
92	3.236	3.236	2.118	1.494	1.494	1.742	-0.248	0.11	0.624
93	3.109	3.109	2.45	1.567	1.567	1.542	0.025	-0.01	0.883
94	3.109		2.238	1.567					0.671
95	3.109		2.014	1.567					0.447
96	3.123	3.123	1.355	1.579	1.579	1.544	0.035	-0.02	-0.224
97	3.123		1.143	1.579					-0.436
98	3.112	3.112	1.981	1.309	1.309	1.803	-0.494	0.25	0.672
99	3.112		1.768	1.309					0.459
100	3.112		1.309	1.309					0

101	3.086	3.086	2.426	1.555	1.555	1.531	0.024	-0.01	0.871
102	3.086		2.203	1.555					0.648
103	3.336	3.336	1.98	1.568	1.568	1.768	-0.2	0.09	0.412
104	3.336		1.768	1.568					0.2
105	3.336		1.568	1.568					0
106	3.336		1.356	1.568					-0.212
107	3.336		1.155	1.568					-0.413
108	3.383	3.383	1.556	1.556	1.556	1.827	-0.271	0.11	0
109	3.348	3.348	1.992	1.356	1.356	1.992	-0.636	0.28	0.636
110	3.348		1.356	1.356					0
111	3.348		1.143	1.356					-0.213
112	3.348		0.931	1.356					-0.425
113	3.535	3.535	2.628	1.756	1.756	1.779	-0.023	0.01	0.872
114	3.535		2.404	1.756					0.648
115	3.535		2.192	1.756					0.436
116	3.535		1.956	1.756					0.2
117	3.107	3.107	1.33	1.33	1.33	1.777	-0.447	0.23	0
118	3.107		1.118	1.33					-0.212
119	3.107		0.894	1.33					-0.436
120	2.862	2.862	1.743	1.107	1.107	1.755	-0.648	0.40	0.636
121	2.862		1.519	1.107					0.412
122	2.862		1.107	1.107					0
123	3.334	3.334	2.427	2.015	2.015	1.319	0.696	-0.32	0.412
124	3.334		2.215	2.015					0.2
125	3.334		2.015	2.015					0
126	3.098	3.098	1.119	1.331	1.331	1.767	-0.436	0.22	-0.212
127	3.098		0.895	1.331					-0.436
128	3.307	3.307	1.801	1.801	1.801	1.506	0.295	-0.13	0
129	3.307		1.577	1.801					-0.224
130	3.275	3.275	2.18	1.532	1.532	1.743	-0.211	0.10	0.648
131	3.275		1.744	1.532					0.212
132	3.275		1.32	1.532					-0.212
133	3.275		1.107	1.532					-0.425
134	3.298	3.298	1.084	1.496	1.496	1.802	-0.306	0.14	-0.412
135	3.039	3.039	1.932	1.519	1.519	1.52	-0.001	0.00	0.413
136	3.039		1.731	1.519					0.212
137	3.039		1.519	1.519					0
138	3.039		1.107	1.519					-0.412

139	3.247	3.247	1.741	1.529	1.529	1.718	-0.189	0.09	0.212
140	3.247		1.529	1.529					0
141	3.247		1.318	1.529					-0.211
142	3.253	3.253	2.157	1.544	1.544	1.709	-0.165	0.08	0.613
143	3.253		1.956	1.544					0.412
144	3.253		1.544	1.544					0
145	3.253		1.343	1.544					-0.201
146	3.253		1.131	1.544					-0.413
147	3.309	3.309	1.531	1.531	1.531	1.778	-0.247	0.11	0
148	3.309		1.307	1.531					-0.224
149	3.25	3.25	1.507	1.719	1.719	1.531	0.188	-0.09	-0.212
150	3.192	3.192	1.59	1.59	1.59	1.602	-0.012	0.01	0
151	3.641	3.641	1.591	1.591	1.591	2.05	-0.459	0.17	0
152	3.641		1.367	1.591					-0.224
153	3.654	3.654	2.275	1.615	1.615	2.039	-0.424	0.16	0.66
154	3.415	3.415	2.061	1.86	1.86	1.555	0.305	-0.13	0.201
155	3.415		1.649	1.86					-0.211
156	3.167	3.167	1.542	1.542	1.542	1.625	-0.083	0.04	0
157	3.179	3.179	0.907	1.542	1.542	1.637	-0.095	0.05	-0.635
158	3.194	3.194	1.815	1.591	1.591	1.603	-0.012	0.01	0.224
159	3.194		1.591	1.591					0
160	3.194		1.379	1.591					-0.212
161	3.428	3.428	2.273	1.826	1.826	1.602	0.224	-0.09	0.447
162	3.189	3.189	1.389	1.601	1.601	1.588	0.013	-0.01	-0.212
163	3.189		1.177	1.601					-0.424
164	2.943	2.943	1.589	1.377	1.377	1.566	-0.189	0.11	0.212
165	2.943		1.377	1.377					0
166	3.427	3.427	1.826	1.826	1.826	1.601	0.225	-0.09	0
167	3.17	3.17	2.039	1.614	1.614	1.556	0.058	-0.03	0.425
168	3.17		1.815	1.614					0.201
169	2.966	2.966	1.601	1.354	1.354	1.612	-0.258	0.14	0.247
170	2.966		1.354	1.354					0
171	3.235	3.235	2.047	1.835	1.835	1.4	0.435	-0.20	0.212
172	3.218	3.218	1.803	1.579	1.579	1.639	-0.06	0.03	0.224
173	3.448	3.448	1.801	1.553	1.553	1.895	-0.342	0.14	0.248
174	3.448		1.553	1.553					0
175	3.235	3.235	2.035	1.565	1.565	1.67	-0.105	0.05	0.47
176	3.235		1.8	1.565					0.235

177	3.203	3.203	1.578	1.331	1.331	1.872	-0.541	0.26	0.247
178	3.203		1.331	1.331					0
179	3.167	3.167	1.154	1.601	1.601	1.566	0.035	-0.02	-0.447
180	3.424	3.424	2.742	1.859	1.859	1.565	0.294	-0.12	0.883
181	3.424		2.518	1.859					0.659
182	3.424		2.071	1.859					0.212
183	3.424		1.859	1.859					0
184	3.168	3.168	2.238	1.343	1.343	1.825	-0.482	0.24	0.895
185	3.168		2.014	1.343					0.671
186	3.168		1.778	1.343					0.435
187	3.423	3.423	1.588	1.388	1.388	2.035	-0.647	0.28	0.2
188	3.2	3.2	1.306	1.306	1.306	1.894	-0.588	0.29	0
189	3.192	3.192	2.274	1.402	1.402	1.79	-0.388	0.19	0.872
190	3.192		2.05	1.402					0.648
191	3.192		1.826	1.402					0.424
192	3.413	3.413	1.801	1.601	1.601	1.812	-0.211	0.09	0.2
193	3.247	3.247	1.376	1.141	1.141	2.106	-0.965	0.48	0.235
194	3.247		1.141	1.141					0
195	3.454	3.454	1.874	1.874	1.874	1.58	0.294	-0.12	0
196	3.451	3.451	1.178	1.414	1.414	2.037	-0.623	0.26	-0.236
197	3.419	3.419	1.379	1.603	1.603	1.816	-0.213	0.09	-0.224
198	3.235	3.235	1.365	1.153	1.153	2.082	-0.929	0.47	0.212
199	3.235		1.153	1.153					0
200	3.235		0.929	1.153					-0.224
201	3.247	3.247	1.847	1.141	1.141	2.106	-0.965	0.48	0.706
202	3.247		1.612	1.141					0.471
203	3.247		1.377	1.141					0.236
204	3.247		1.141	1.141					0
205	3.472	3.472	2.554	1.636	1.636	1.836	-0.2	0.08	0.918
206	3.472		2.319	1.636					0.683
207	3.472		2.095	1.636					0.459
208	3.447	3.447	1.8	1.365	1.365	2.082	-0.717	0.30	0.435
209	3.447		1.365	1.365					0
210	3.229	3.229	1.178	1.614	1.614	1.615	-0.001	0.00	-0.436
211	2.969	2.969	1.402	1.637	1.637	1.332	0.305	-0.17	-0.235
212	2.969		1.178	1.637					-0.459
213	3.393	3.393	2.486	1.567	1.567	1.826	-0.259	0.11	0.919
214	3.393		2.25	1.567					0.683

215	3.404	3.404	2.05	1.826	1.826	1.578	0.248	-0.10	0.224
216	3.404		1.826	1.826					0
217	3.723	3.723	1.85	1.64	1.64	2.083	-0.443	0.16	0.21
218	3.723		1.64	1.64					0
219	3.723		1.402	1.64					-0.238
220	3.472	3.472	2.071	1.601	1.601	1.871	-0.27	0.11	0.47
221	3.259	3.259	1.835	1.376	1.376	1.883	-0.507	0.24	0.459
222	3.259		1.612	1.376					0.236
223	3.271	3.271	1.376	1.165	1.165	2.106	-0.941	0.46	0.211
224	3.271		0.941	1.165					-0.224
225	3.248	3.248	2.542	1.612	1.612	1.636	-0.024	0.01	0.93
226	3.248		2.318	1.612					0.706
227	3.248		2.083	1.612					0.471
228	3.248		1.847	1.612					0.235
229	3.461	3.461	1.848	2.072	2.072	1.389	0.683	-0.29	-0.224
230	3.201	3.201	2.048	1.812	1.812	1.389	0.423	-0.20	0.236
231	2.993	2.993	1.39	1.39	1.39	1.603	-0.213	0.12	0
232	3.016	3.016	1.178	1.637	1.637	1.379	0.258	-0.14	-0.459
233	3.52	3.52	1.613	1.613	1.613	1.907	-0.294	0.12	0
234	3.448	3.448	1.86	1.86	1.86	1.588	0.272	-0.11	0
235	3.448		1.624	1.86					-0.236
236	3.448		1.401	1.86					-0.459
237	3.217	3.217	1.815	1.379	1.379	1.838	-0.459	0.22	0.436
238	3.217		1.591	1.379					0.212
239	3.217		1.155	1.379					-0.224
240	3.461	3.461	1.813	1.577	1.577	1.884	-0.307	0.12	0.236
241	3.461		1.577	1.577					0
					$d_{l(\text{ave})}$ [nm]	$d_{u(\text{ave})}$ [nm]	$d_{l-u(\text{ave})}$ [nm]	$D_{\text{net}(\text{ave})}$ [mJ/m <sup>2</sup> ]	
					<b>1.569</b>	<b>1.688</b>	<b>-0.119</b>	<b>0.05</b>	

Table S2. Numerical data of various number of layers for the 0.4-sample, corresponding to Table S1. Deletion of duplicates is due to the presence of two or more dislocations in a single line profile. The sample numbers of Fig. 4(e) in the main text are rearranged in order of increasing number of  $N_{d\text{-Co}}$  to make the distribution of the dislocation layers relative to the highest Co layer easier to recognize.

Sample number	Number of layers from the bottom to top highest Pt layer	Remove duplicates from the left column	Layer position of the highest Co layer counting from the bottom highest Pt layer	Remove duplicates from the left column	Layer position of the dislocation layer counting from the bottom highest Pt layer	Layer difference between $N_d$ and $N_{Co}$ [Fig. 4(e)]
	$N_{Pt\text{-Pt}}$ [number]	$N_{Pt\text{-Pt}}$ [number]	$N_{Co}$ [number]	$N_{Co}$ [number]	$N_d$ [number]	$N_{d\text{-Co}}$ [number]
1	15	15	9	9	11	2
2	15		9		10	1
3	16	16	9	9	8	-1
4	16		9		7	-2
5	16	16	9	9	13	4
6	16		9		12	3
7	17	17	8	8	9	1
8	17	17	8	8	11	3
9	17		8		10	2
10	17		8		9	1
11	17		8		8	0
12	17		8		7	-1
13	16	16	8	8	11	3
14	16		8		10	2
15	16		8		9	1
16	15	15	7	7	8	1
17	15		7		7	0
18	15		7		6	-1
19	15	15	7	7	7	0
20	15		7		6	-1
21	16	16	8	8	13	5
22	16		8		12	4
23	16		8		10	2
24	16		8		8	0
25	16		8		7	-1
26	16		8		6	-2
27	15	15	8	8	11	3
28	15		8		10	2

29	15		8		9	1
30	15	15	8	8	10	2
31	14	14	7	7	6	-1
32	14		7		5	-2
33	16	16	8	8	6	-2
34	16	16	8	8	7	-1
35	15	15	7	7	8	1
36	15		7		7	0
37	15	15	7	7	7	0
38	15		7		6	-1
39	15		7		5	-2
40	14	14	7	7	8	1
41	16	16	8	8	11	3
42	16		8		10	2
43	16		8		9	1
44	16		8		6	-2
45	16	16	9	9	12	3
46	16		9		11	2
47	16		9		10	1
48	16	16	9	9	9	0
49	16	16	8	8	11	3
50	16		8		9	1
51	16	16	8	8	6	-2
52	15	15	7	7	7	0
53	16	16	8	8	8	0
54	14	14	7	7	9	2
55	14		7		6	-1
56	14		7		5	-2
57	15	15	8	8	11	3
58	15	15	7	7	6	-1
59	16	16	9	9	9	0
60	16	16	8	8	11	3
61	16		8		10	2
62	16		8		9	1
63	16	16	8	8	8	0
64	16		8		7	-1
65	16	16	9	9	12	3
66	16		9		11	2

67	16		9		10	1
68	16	16	9	9	11	2
69	16		9		9	0
70	16	16	10	10	13	3
71	16		10		12	2
72	16		10		10	0
73	16		10		9	-1
74	16	16	8	8	7	-1
75	16	16	9	9	9	0
76	15	15	8	8	8	0
77	15		8		7	-1
78	15		8		6	-2
79	15	15	9	9	11	2
80	15		9		10	1
81	16	16	9	9	10	1
82	15	15	9	9	12	3
83	15	15	8	8	10	2
84	15		8		7	-1
85	15	15	8	8	11	3
86	15		8		10	2
87	15		8		9	1
88	17	17	8	8	8	0
89	17		8		7	-1
90	15	15	9	9	10	1
91	15		9		9	0
92	16	16	8	8	11	3
93	15	15	8	8	12	4
94	15		8		11	3
95	15		8		10	2
96	15	15	8	8	7	-1
97	15		8		6	-2
98	15	15	7	7	10	3
99	15		7		9	2
100	15		7		7	0
101	15	15	8	8	12	4
102	15		8		11	3
103	16	16	8	8	10	2
104	16		8		9	1

105	16		8		8	0
106	16		8		7	-1
107	16		8		6	-2
108	16	16	8	8	8	0
109	16	16	7	7	10	3
110	16		7		7	0
111	16		7		6	-1
112	16		7		5	-2
113	17	17	9	9	13	4
114	17		9		12	3
115	17		9		11	2
116	17		9		10	1
117	15	15	7	7	7	0
118	15		7		6	-1
119	15		7		5	-2
120	14	14	6	6	9	3
121	14		6		8	2
122	14		6		6	0
123	16	16	10	10	12	2
124	16		10		11	1
125	16		10		10	0
126	15	15	7	7	6	-1
127	15		7		5	-2
128	16	16	9	9	9	0
129	16		9		8	-1
130	16	16	8	8	11	3
131	16		8		9	1
132	16		8		7	-1
133	16		8		6	-2
134	16	16	8	8	6	-2
135	15	15	8	8	10	2
136	15		8		9	1
137	15		8		8	0
138	15		8		6	-2
139	16	16	8	8	9	1
140	16		8		8	0
141	16		8		7	-1
142	16	16	8	8	11	3

143	16		8		10	2
144	16		8		8	0
145	16		8		7	-1
146	16		8		6	-2
147	16	16	8	8	8	0
148	16		8		7	-1
149	16	16	9	9	8	-1
150	15	15	8	8	8	0
151	17	17	8	8	8	0
152	17		8		7	-1
153	17	17	8	8	11	3
154	16	16	9	9	10	1
155	16		9		8	
156	15	15	8	8	8	0
157	15	15	8	8	5	-3
158	15	15	8	8	9	1
159	15		8		8	0
160	15		8		7	-1
161	16	16	9	9	11	2
162	15	15	8	8	7	-1
163	15		8		6	-2
164	14	14	7	7	8	1
165	14		7		7	0
166	16	16	9	9	9	0
167	15	15	8	8	10	2
168	15		8		9	1
169	14	14	7	7	8	1
170	14		7		7	0
171	15	15	9	9	10	1
172	15	15	8	8	9	1
173	16	16	8	8	9	1
174	16		8		8	0
175	15	15	8	8	10	2
176	15		8		9	1
177	15	15	7	7	8	1
178	15		7		7	0
179	15	15	8	8	6	-2
180	16	16	9	9	13	4

181	16		9		12	3
182	16		9		10	1
183	16		9		9	0
184	15	15	7	7	11	4
185	15		7		10	3
186	15		7		9	2
187	16	16	7	7	8	1
188	15	15	7	7	7	0
189	15	15	7	7	11	4
190	15		7		10	3
191	15		7		9	2
192	16	16	8	8	9	1
193	15	15	6	6	7	1
194	15		6		6	0
195	16	16	9	9	9	0
196	16	16	9	9	8	-1
197	16	16	8	8	7	-1
198	15	15	6	6	7	1
199	15		6		6	0
200	15		6		5	-1
201	15	15	6	6	9	3
202	15		6		8	2
203	15		6		7	1
204	15		6		6	0
205	16	16	8	8	12	4
206	16		8		11	3
207	16		8		10	2
208	16	16	7	7	9	2
209	16		7		7	0
210	15	15	8	8	6	-2
211	14	14	8	8	7	-1
212	14		8		6	-2
213	16	16	8	8	12	4
214	16		8		11	3
215	16	16	9	9	10	1
216	16		9		9	0
217	17	17	8	8	9	1
218	17		8		8	0

219	17		8		7	-1
220	16	16	8	8	10	2
221	15	15	7	7	9	2
222	15		7		8	1
223	15	15	6	6	7	1
224	15		6		5	-1
225	15	15	8	8	12	4
226	15		8		11	3
227	15		8		10	2
228	15		8		9	1
229	16	16	10	10	9	-1
230	15	15	9	9	10	1
231	14	14	7	7	7	0
232	14	14	8	8	6	-2
233	16	16	8	8	8	0
234	16	16	9	9	9	0
235	16		9		8	-1
236	16		9		7	-2
237	15	15	7	7	9	2
238	15		7		8	1
239	15		7		6	-1
240	16	16	8	8	9	1
241	16		8		8	0

Table S3. Numerical data of various distance measurements and number of layers for the 1.0-sample. The reason why half-integers are shown in  $N_{Co}$  is that the middle of the adjacent highest Co layers is defined as the virtual highest Co layer. The sample numbers of Fig. 3(b) in the main text are rearranged in order of increasing  $d_{l-u}$  value to make the dispersion easier to recognize.

Sample number	Distance between highest Pt at top and bottom	Distance of the highest Co from the bottom highest Pt [Fig. 3(b)]	Distance of the highest Co from the top highest Pt [Fig. 3(b)]	Distance between $d_l$ and $d_u$	Net Bulk DMI energy [Fig. 3(d)]	Number of layers from the bottom to top highest Pt layer	Layer position of the highest Co layer counting from the bottom highest Pt layer
	$d_{Pt-Pt}$ [nm]	$d_l$ [nm]	$d_u$ [nm]	$d_{l-u}$ [nm]	$D_{net}$ [mJ/m <sup>2</sup> ]	$N_{Pt-Pt}$ [number]	$N_{Co}$ [number]
1	2.599	1.092	1.506	-0.414	0.30	13	6
2	2.806	1.280	1.525	-0.245	0.15	14	7

3	2.617	1.064	1.554	-0.490	0.36	13	6
4	2.843	1.337	1.506	-0.169	0.10	14	7
5	2.843	1.337	1.506	-0.169	0.10	14	7
6	2.843	1.318	1.525	-0.207	0.12	14	7
7	2.655	0.904	1.544	-0.640	0.55	13	5.5
8	2.617	1.101	1.515	-0.414	0.30	13	6
9	2.645	1.148	1.497	-0.348	0.24	13	6
10	3.012	1.271	1.741	-0.470	0.26	15	7
11	3.012	1.252	1.760	-0.508	0.28	15	7
12	2.579	1.064	1.515	-0.452	0.34	13	6
13	2.976	1.394	1.582	-0.188	0.10	14	7
14	2.665	1.318	1.347	-0.028	0.02	13	7
15	3.116	1.337	1.779	-0.443	0.22	15	7
16	3.032	1.497	1.535	-0.038	0.02	15	8
17	3.182	1.798	1.384	0.414	-0.20	15	9
18	3.107	1.544	1.563	-0.019	0.01	15	8
19	2.871	1.732	1.139	0.593	-0.36	14	9
20	3.154	1.318	1.601	-0.283	0.16	15	7.5
21	3.136	1.507	1.629	-0.123	0.06	15	8
22	3.117	1.507	1.610	-0.104	0.05	15	8
23	2.872	1.525	1.346	0.179	-0.11	14	8
24	2.871	1.525	1.346	0.179	-0.11	14	8
25	3.069	1.516	1.553	-0.038	0.02	15	8
26	2.890	1.572	1.318	0.254	-0.15	14	8
27	3.333	1.742	1.591	0.151	-0.07	16	9
28	2.890	1.299	1.591	-0.292	0.17	14	7
29	2.928	1.563	1.365	0.198	-0.11	14	8
30	2.890	1.534	1.356	0.179	-0.10	14	8
31	2.881	1.553	1.327	0.226	-0.13	14	8
32	3.078	1.534	1.544	-0.010	0.00	15	8
33	2.908	1.337	1.327	0.010	-0.01	14	7.5
34	2.918	1.177	1.544	-0.367	0.24	14	6.5
35	3.022	1.440	1.365	0.075	-0.05	14	7.5
36	3.136	1.591	1.544	0.047	-0.02	15	8
37	2.776	1.619	1.158	0.461	-0.30	13	8
38	2.899	1.798	1.101	0.696	-0.42	14	9
39	3.096	1.562	1.299	0.264	-0.16	15	8.5
40	2.937	1.581	1.355	0.226	-0.13	14	8

41	2.918	1.346	1.572	-0.226	0.13	14	7
42	2.664	1.111	1.337	-0.226	0.18	13	6.5
43	2.654	1.120	1.534	-0.414	0.29	13	6
44	2.918	1.129	1.788	-0.659	0.39	14	6
45	2.927	1.402	1.525	-0.122	0.07	14	7
46	2.937	1.374	1.562	-0.188	0.11	14	7
47	2.918	1.356	1.563	-0.207	0.12	14	7
48	2.721	1.374	1.346	0.028	-0.02	13	7
49	3.154	1.394	1.761	-0.367	0.18	15	7
50	3.145	1.563	1.356	0.207	-0.12	15	8.5
51	2.721	1.375	1.111	0.264	-0.21	13	7.5
52	2.712	1.346	1.130	0.217	-0.17	13	7.5
53	2.712	1.347	1.140	0.207	-0.16	13	7.5
54	2.467	0.876	1.592	-0.716	0.62	12	5
55	2.899	1.082	1.544	-0.461	0.33	14	6.5
56	2.443	1.120	1.087	0.033	-0.03	12	6.5
57	2.890	1.562	1.327	0.235	-0.14	14	8
58	2.927	1.591	1.337	0.254	-0.14	14	8
59	2.976	1.799	1.177	0.622	-0.35	14	9
60	2.948	1.582	1.121	0.462	-0.31	14	8.5
61	3.004	1.620	1.121	0.499	-0.33	14	8.5
62	2.656	1.601	1.055	0.546	-0.39	13	8
63	3.136	1.591	1.544	0.047	-0.02	15	8
64	3.146	1.582	1.347	0.235	-0.13	15	8.5
65	2.929	1.356	1.356	0.000	0.00	14	7.5
66	2.843	1.346	1.280	0.066	-0.05	14	7.5
67	2.862	1.158	1.506	-0.348	0.24	14	6.5
68	2.401	1.328	0.885	0.443	-0.45	12	7.5
69	2.844	1.102	1.742	-0.640	0.40	14	6
70	3.098	1.592	1.507	0.085	-0.04	15	8
71	2.891	1.356	1.535	-0.179	0.10	14	7
72	3.040	1.751	1.289	0.461	-0.25	15	9
73	2.861	1.299	1.562	-0.264	0.16	14	7
74	3.332	1.572	1.760	-0.188	0.08	16	8
75	2.861	1.327	1.308	0.019	-0.01	14	7.5
76	2.618	1.347	1.271	0.075	-0.05	13	7
77	3.249	1.733	1.516	0.217	-0.10	16	9
78	2.655	1.328	1.111	0.217	-0.18	13	7.5

79	3.324	1.554	1.563	-0.009	0.00	16	8.5
80	2.927	1.365	1.563	-0.198	0.11	14	7
81	3.116	1.553	1.337	0.216	-0.13	15	8.5
82	2.673	1.111	1.346	-0.235	0.19	13	6.5
83	3.379	1.581	1.591	-0.009	0.00	16	8.5
84	3.408	1.883	1.346	0.537	-0.26	16	9.5
85	2.485	1.158	1.111	0.047	-0.04	12	6.5
86	2.946	1.600	1.346	0.254	-0.14	14	8
87	3.135	1.591	1.327	0.264	-0.15	15	8.5
88	2.937	1.365	1.365	0.000	0.00	14	7.5
89	3.013	1.375	1.638	-0.264	0.14	14	7
90	3.098	1.460	1.394	0.066	-0.04	14	7.5
91	3.013	1.441	1.573	-0.132	0.07	14	7
92	2.805	1.205	1.600	-0.395	0.25	13	6
93	3.248	1.648	1.600	0.047	-0.02	15	8
94	3.003	1.638	1.365	0.273	-0.15	14	8
95	2.975	1.422	1.327	0.094	-0.06	14	7.5
96	2.984	1.167	1.572	-0.405	0.27	14	6.5
97	3.013	1.873	1.139	0.734	-0.41	14	9
98	2.523	0.932	1.346	-0.414	0.40	12	5.5
99	2.542	1.158	1.384	-0.226	0.17	12	6
100	3.012	1.657	1.355	0.301	-0.16	14	8
101	2.562	1.187	1.375	-0.188	0.14	12	6
102	2.298	0.951	1.111	-0.160	0.18	11	5.5
103	3.249	1.158	1.846	-0.688	0.39	15	6.5
104	2.995	1.394	1.601	-0.207	0.11	14	7
105	2.505	1.337	1.168	0.170	-0.13	12	7
106	2.806	1.177	1.384	-0.207	0.15	13	6.5
107	2.730	1.563	1.167	0.396	-0.26	13	8
108	2.777	1.149	1.384	-0.235	0.18	13	6.5
109	2.909	1.365	1.544	-0.179	0.10	14	7
110	2.946	1.393	1.318	0.075	-0.05	14	7.5
111	2.975	1.167	1.807	-0.640	0.37	14	6
112	2.946	1.158	1.789	-0.631	0.37	14	6
113	2.956	1.836	1.120	0.715	-0.42	14	9
114	3.107	1.516	1.346	0.169	-0.10	15	8.5
115	2.900	1.290	1.365	-0.075	0.05	14	7.5
116	3.135	1.309	1.582	-0.273	0.16	15	7.5

117	2.899	1.337	1.563	-0.226	0.13	14	7
118	2.946	1.139	1.591	-0.452	0.30	14	6.5
119	2.730	1.120	1.384	-0.264	0.20	13	6.5
120	2.683	1.111	1.337	-0.226	0.18	13	6.5
121	2.494	1.130	1.130	0.000	0.00	12	6.5
122	2.946	1.403	1.544	-0.141	0.08	14	7
		$d_{l(\text{ave})}$ [nm]	$d_{u(\text{ave})}$ [nm]	$d_{l-u(\text{ave})}$ [nm]	$D_{\text{net}(\text{ave})}$ [mJ/m <sup>2</sup> ]		
		1.388	1.427	-0.039	0.03		

### III. Separation distance between the positions of highest Co and dislocations for the 0.4-sample

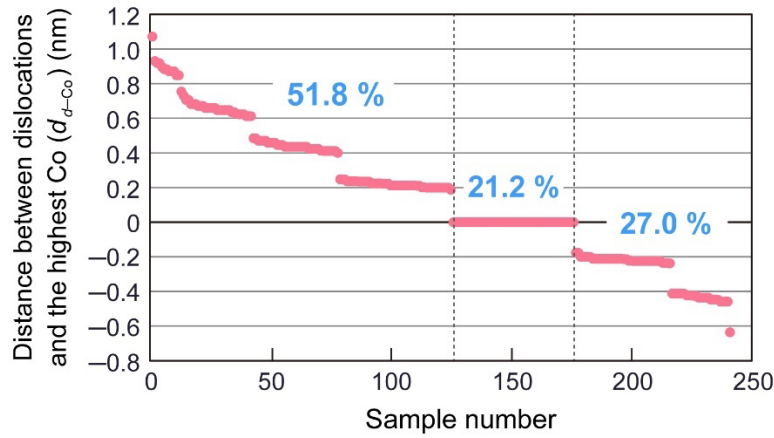


FIG. S2. Separation distance  $d_{d-\text{Co}}$  between the positions of the highest Co and dislocations for the 0.4-sample. This figure corresponds to Fig. 4(e) in the main text. The numerical data are listed in Table S1.

### IV. Measurements of spin-orbit coupling by electron energy loss spectroscopy for the 0.4- and 1.0-samples

Electron energy loss spectroscopy (EELS) can provide a direct measure of the effective spin-orbit coupling (SOC) of Co. The core-loss spectra obtained from EELS can provide the same information as X-ray Absorption Spectroscopy (XAS) spectra. Recent XAS studies on Co-based and Fe-based multilayers have demonstrated an enhanced SOC in the local electronic structures of Co and Fe by measuring the branching ratio  $B$ . This ratio is defined as the fraction of the total XAS intensity  $I$  at the  $L_3$  edge, denoted as  $B = I(L_3)/[I(L_3) + I(L_2)]$  [S1-S4]. This branching ratio is theoretically defined as  $B = B_0 + \langle l \cdot s / n_h \rangle$ , where  $B_0$  is the branching ratio without SOC,  $l$  and  $s$  are the orbital and spin angular momentum, respectively, and  $n_h$  is the number of  $d$ -holes [S5]. We conducted EELS measurements for the 0.4- and 1.0-samples. We used TEM-EELS mode to measure the core-loss spectra obtained from the whole regions in the 0.4- and 1.0-samples, as shown in Figs. S3(a) and S3(b), respectively. Even though the 1.0-sample exhibits a substantial net bulk DMI, the peak intensity of the 1.0-sample is nearly identical to that of the 0.4-sample. The branching ratio for the 0.4- and 1.0-samples is

$B \approx 0.67$ , which is significantly smaller than the enhanced branching ratio of  $B = 0.75\text{-}0.82$  obtained in previous studies of spin-orbit torque in multilayers [S1,S2,S4] and is almost ideal in Co without SOC (the integrated intensity ratio  $I(L_3)/I(L_2)$  is equal to 2/1). We also used STEM-EELS mode to measure the core-loss spectra obtained from the grain boundary in the 0.4-sample, as shown in Fig. S3(c). The reason for examining the grain boundary in the 0.4-sample instead of the 1.0-sample is that the grain of the 0.4-sample is larger than that of the 1.0 sample, and core-loss spectra can be reliably obtained from the grain boundary only. However, the intensity and shape of the core-loss spectra obtained from the grain boundaries are not much different from those obtained from the whole sample [Fig. S3(a)], with the branching ratio of  $B \approx 0.67$ . Based on these results, we conclude that the effective SOC of the 1.0-sample with the substantial net bulk DMI is not significantly different from that of the 0.4 sample.

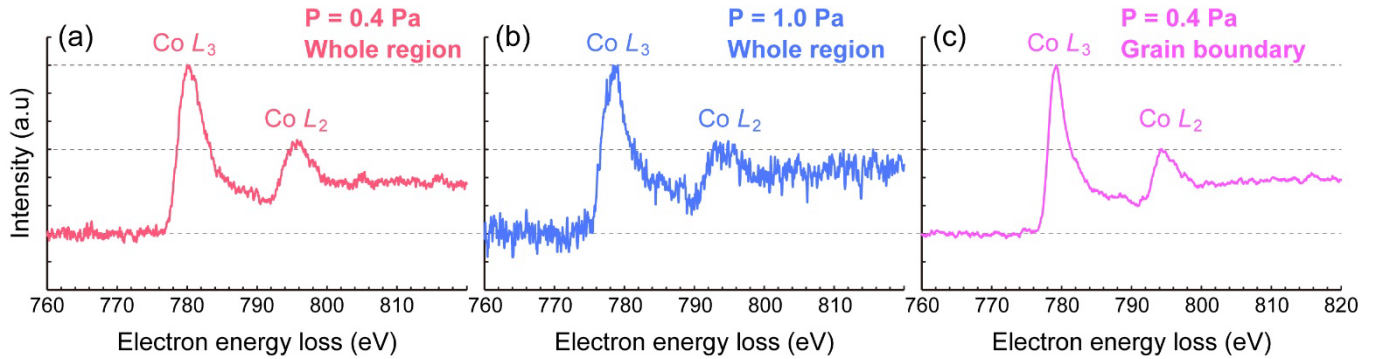


FIG. S3. Core-loss spectra in EELS obtained from the whole region of the 0.4-sample (a) and the 1.0-sample (b), and a grain boundary in the 0.4-sample (c). All spectra show nearly the same intensity and shape. The poor S/N ratio in (b) is probably because the thickness of the 1.0-sample is thicker than that of the 0.4-sample.

## References

- The reference [S1]-[S4] below are identical to the references [49]-[52] in the main text.
- [S1] J. W. Lee, Y.-W. Oh, S.-Y. Park, A. I. Figueroa, G. van der Laan, G. Go, K.-J. Lee, and B.-G. Park, Enhanced spin-orbit torque by engineering Pt resistivity in Pt/Co/AlO<sub>x</sub> structures, Phys. Rev. B **96**, 064405 (2017).
  - [S2] R. Wang, Z. Xiao, H. Liu, Z. Quan, X. Zhang, M. Wang, M. Wu, and X. Xu, Enhancement of perpendicular magnetic anisotropy and spin-orbit torque in Ta/Pt/Co/Ta multi-layered heterostructures through interfacial diffusion, Appl. Phys. Lett. **114**, 042404 (2019).
  - [S3] D. K. Ojha, R. Chatterjee, Y.-L. Lin, Y.-H. Wu, P.-W. Chen, and Y.-C. Tseng, Spin-torque efficiency enhanced in sputtered topological insulator by interface engineering, J. Magn. Magn. Mater. **572**, 170638 (2023).
  - [S4] L. Chen, K. Zhang, B. Li, B. Hong, W. Huang, Y. He, X. Feng, Z. Zhang, K. Lin, W. Zhao, and Y. Zhang, Engineering Symmetry Breaking Enables Efficient Bulk Spin-Orbit Torque-Driven Perpendicular Magnetization Switching, Adv. Funct. Mater. **34**, 2308823 (2023).
  - [S5] B. T. Thole and G. van der Laan, Branching ratio in x-ray absorption spectroscopy, Phys. Rev. B **38**, 3158 (1988).